agriculture

MDPI

Article

Winter Wheat SPAD Prediction Based on Multiple Preprocessing, Sequential Module Fusion, and Feature Mining Methods

Ying Nian [1], Xiangxiang Su [1], Hu Yue [1], Sumera Anwar [2], Jun Li [1], Weiqiang Wang [1], Yali Sheng [1], Qiang Ma [1], Jikai Liu [1,3] and Xinwei Li [1,3,*]

[1] College of Resource and Environment, Anhui Science and Technology University, Chuzhou 233100, China; nianying1010@163.com (Y.N.); suxxahstu@163.com (X.S.); yuehahstu@163.com (H.Y.); lijahstu@163.com (J.L.); w000910@163.com (W.W.); shengyali333@163.com (Y.S.); maq@ahstu.edu.cn (Q.M.); liujk@ahstu.edu.cn (J.L.)
[2] Department of Botany, Government College Women University Faisalabad, Faisalabad 38000, Pakistan; sumeraanwar@mail.hzau.edu.cn
[3] Anhui Province Crop Intelligent Planting and Processing Technology Engineering Research Center, Chuzhou 233100, China
* Correspondence: lixw@ahstu.edu.cn

Abstract: Chlorophyll is a crucial indicator for monitoring crop growth and assessing nutritional status. Hyperspectral remote sensing plays an important role in precision agriculture, offering a non-destructive approach to predicting leaf chlorophyll. However, crop canopy spectra often face background noise and data redundancy challenges. To tackle these issues, this study develops an integrated processing strategy incorporating multiple preprocessing techniques, sequential module fusion, and feature mining methods. Initially, the original spectrum (OS) from 2021, 2022, and the fusion year underwent preprocessing through Fast Fourier Transform (FFT) smoothing, multiple scattering correction (MSC), the first derivative (FD), and the second derivative (SD). Secondly, feature mining was conducted using Competitive Adaptive Reweighted Sampling (CARS), Iterative Retention of Information Variables (IRIV), and Principal Component Analysis (PCA) based on the optimal preprocessing order module fusion data. Finally, Partial Least Squares Regression (PLSR) was used to construct a prediction model for winter wheat SPAD to compare the prediction effects in different years and growth stages. The findings show that the preprocessing sequential module fusion of FFT-MSC (firstly pre-processing using FFT, and secondly secondary processing of FFT spectral data using MSC) effectively reduced issues such as noisy signals and baseline drift. The FFT-MSC-IRIV-PLSR model (based on the combined FFT-MSC preprocessed spectral data, feature screening using IRIV, and then combining with PLSR to construct a prediction model) predicts SPAD with the highest overall accuracy, with an R^2 of 0.79–0.89, RMSE of 4.51–5.61, and MAE of 4.01–4.43. The model performed best in 2022, with an R^2 of 0.84–0.89 and RMSE of 4.51–6.74. The best prediction during different growth stages occurred in the early filling stage, with an R^2 of 0.75 and RMSE of 0.58. On the basis of this research, future work will focus on optimizing the data processing process and incorporating richer environmental data, so as to further enhance the predictive capability and applicability of the model.

Keywords: hyperspectral; winter wheat; chlorophyll; feature mining methods; preprocessing methods

check for updates

Citation: Nian, Y.; Su, X.; Yue, H.; Anwar, S.; Li, J.; Wang, W.; Sheng, Y.; Ma, Q.; Liu, J.; Li, X. Winter Wheat SPAD Prediction Based on Multiple Preprocessing, Sequential Module Fusion, and Feature Mining Methods. *Agriculture* **2024**, *14*, 2258. https://doi.org/10.3390/agriculture14122258

Received: 1 November 2024
Revised: 27 November 2024
Accepted: 7 December 2024
Published: 10 December 2024

Copyright: © 2024 by the authors. Licensee MDPI, Basel, Switzerland. This article is an open access article distributed under the terms and conditions of the Creative Commons Attribution (CC BY) license (https://creativecommons.org/licenses/by/4.0/).

1. Introduction

Wheat is one of China's most important grain crops and is essential in ensuring food security [1]. Chlorophyll is a crucial molecule in promoting plant photosynthesis and is closely related to crop health and nitrogen fertilizer use efficiency, which can directly affect wheat yield [2]. Therefore, rapid, non-destructive, and accurate acquisition of leaf chlorophyll information is essential for agricultural production management [3].

Traditional chlorophyll measurement methods, such as acetone extraction and fluorescence analysis, are both a safety risk and cumbersome and challenging to promote [4]. In recent years, remote sensing technology has become a powerful tool for monitoring crop growth in precision agriculture because of its efficiency and convenience [5]. It provides technical support for real-time and accurate acquisition of chlorophyll information [6]. Currently, remote sensing platforms such as satellite platforms [7], near-Earth hyperspectral platforms [8], and unmanned aerial vehicle (UAV) platforms [9] are widely used to assess the physiological and biochemical parameters of crops [10–12]. Satellite platforms are usually used for large-scale regional monitoring, but the spatial resolution is low and susceptible to weather impacts, making it challenging to conduct refined research [13]. Unmanned aerial vehicles (UAVs) are inexpensive and easy to operate but are limited by endurance and face challenges in realizing large-scale and long-time monitoring [14]. Compared with these two platforms, near-surface hyperspectroscopy, which can acquire continuous narrow bands, can identify the reflectance and absorption properties of wheat chlorophyll in different wavelength ranges, and can capture subtle wavelength variations in the canopy reflectance spectra using its high spectral resolution. This approach shows great potential in crop chlorophyll monitoring, providing richer spectral data for chlorophyll monitoring [15,16].

Canopy hyperspectral prediction of wheat chlorophyll is susceptible to interference from random noise, light source noise, and multiple scattering [17]. To reduce the impact of noise on chlorophyll monitoring, a large number of studies have used preprocessing methods such as FFT filtering [18], MSC [19], FD [20], and SD [21] to solve such problematic interferences. FFT can significantly improve the data quality by identifying and filtering frequency-specific noise components in the frequency domain [22]. MSC can effectively resolve the spectral data affected by scattering effects and improve the purity of spectral signals [23]. Moreover, FD and SD can highlight peaks and valleys in spectral signals and analyze changes and trends in spectral curves [24,25]. For example, Singh et al. [26] acquired canopy spectral data of 17 crops using a hyperspectral imaging spectrometer (AVIRIS-NG) and evaluated the performance of three denoising techniques, the FFT filter, the mean filter, and SG smoothing, and the results showed that the FFT filter performed the best. Zhang et al. [27] investigated the relationship between chlorophyll content and spectral data of winter wheat. They used preprocessing methods such as MSC and standard normal variable transformation (SNV) to eliminate the light-scattering effect due to the inconsistency in the size of the solid particles on the wheat leaves, which serves the purpose of correcting the canopy spectra. Zhou et al. [28] used FD, SD, and MSC to preprocess the Vis-NIR spectra of lettuce and combined it with various regression algorithms to construct the SPAD prediction model, which had good prediction results ($R^2 > 0.80$).

The background noise problem in canopy spectra is challenging to solve using a single method. Ollinger et al. [29] showed that plant canopy reflectance variations are affected by multiple factors, such as physiological structure, leaf pigment types, nitrogen, and proteins, which may generate different types of noise affecting the estimation of plant physicochemical parameters. Therefore, integrating different preprocessing methods is necessary to attenuate the effects of multi-source noise [30]. In addition to noise interference, canopy spectral data have problems such as high dimensionality and redundancy [31]. Deep mining of the characteristic bands that are highly correlated with chlorophyll provides a possibility to address these issues [32–34]. For example, Jin et al. [35] showed that the bands within the blue and red light regions contain rich plant phenotypic information, which is highly correlated with the biochemical properties of chlorophyll and provides reliable data for accurate estimation of leaf chlorophyll content. Zhang et al. [36] revealed that the red-edge region is extremely sensitive to changes in plant chlorophyll content and that it is possible to capture fluctuations in the position of the red edge, and thus track changes in chlorophyll content at different growth stages. Buschmann et al. [37] pointed out that leaf chlorophyll is more absorptive and, therefore, less reflective in the 400~500 nm band range.

The above studies have shown that using sensitive bands for chlorophyll prediction is conducive to reducing the complexity of prediction model construction, on the one hand, and facilitating the scientific interpretation of the relationship between canopy spectra and chlorophyll, on the other [38]. Therefore, using suitable feature mining methods to obtain sensitive bands plays a key role in predicting wheat chlorophyll [39]. For example, CARS aims to select the optimal bands that are highly correlated with the target variable from the raw spectral data. The core idea is based on a competitive elimination mechanism that gradually eliminates redundant bands with little or no correlation with the target variable in each iteration, thus improving the generalization ability of the model [40]. IRIV, as a feature selection algorithm with heuristic search, avoids the local optimum problem that may be brought about when selecting feature bands directly from high-dimensional data through random sampling and step-by-step optimization, and ultimately retains the feature bands that are the most useful for the target variables [41].

PCA converts the original spectral data into a set of mutually orthogonal principal components through linear transformation, which can simplify the data structure and improve the model's computational efficiency while retaining the original data's basic information [42]. The above methods have also been widely used in previous studies. For example, Sudu et al. [43] acquired hyperspectral data of different growth stages of summer maize based on UAV hyperspectral data, and then used the feature selection algorithms CARS and RFE to select the feature bands and compared the SPAD prediction accuracy with different machine learning algorithms. Yuan et al. [44] used three methods, the correlation coefficient, CARS, and IRIV, to select the characteristic bands and construct a prediction model for the SPAD value of chili peppers, of which the IRIV model had the highest accuracy, with $R^2 \geq 0.80$. Shen et al. [45] took winter wheat as the research object to compare the performance of the SPAD prediction model constructed from the original data and the spectral data after dimensionality reduction by the feature extraction technique PCA, and the results showed that the sensitive features can significantly improve the model accuracy.

In summary, previous studies lacked systematic exploration of the fusion of different sequential modules of multiple preprocessing methods, which may be defective regarding the noise reduction effect. Meanwhile, although the application of feature mining methods has been widely reported [46,47], the potential of combining different sequential modules of multiple preprocessing fusion methods for predicting crop chlorophyll is not yet known. Therefore, this study mainly proposes an integrated processing strategy that utilizes the fusion of different sequential modules of multiple preprocessing methods (FFT, MSC, FD, SD) combined with feature mining methods (the feature selection algorithms CARS and IRIV, and the feature extraction technique PCA) to solve the problems of crop canopy spectral noise interference and data processing complexity, to improve the effectiveness of wheat SPAD prediction. The research objectives are as follows: (1) to explore the model performance under the fusion of a single preprocessing method and the fusion of different sequential modules of multiple preprocessing methods; (2) to evaluate the effectiveness of two types of feature mining methods for predicting SPAD in wheat; and (3) to compare the differences in SPAD prediction accuracy across years and growth stages.

2. Materials and Methods

2.1. Experimental Site

The experimental site was situated in Xiaogang Village (117°46′7″ E, 32°48′52″ N), located in Chuzhou City, Anhui Province, China (Figure 1). This region experiences a warm-temperate semi-moist monsoon climate characterized by abundant sunshine and distinct monsoon seasons. The experiment was conducted over 2021 and 2022, during which the average annual temperature ranged from 14 to 16 °C, the average annual precipitation fell between 1000 and 1100 mm, and the average annual sunshine duration was between 1800 and 2500 h. Furthermore, Xiaogang Village features flat terrain and moderate soil fertility, making it a significant experimental base for grain crops.

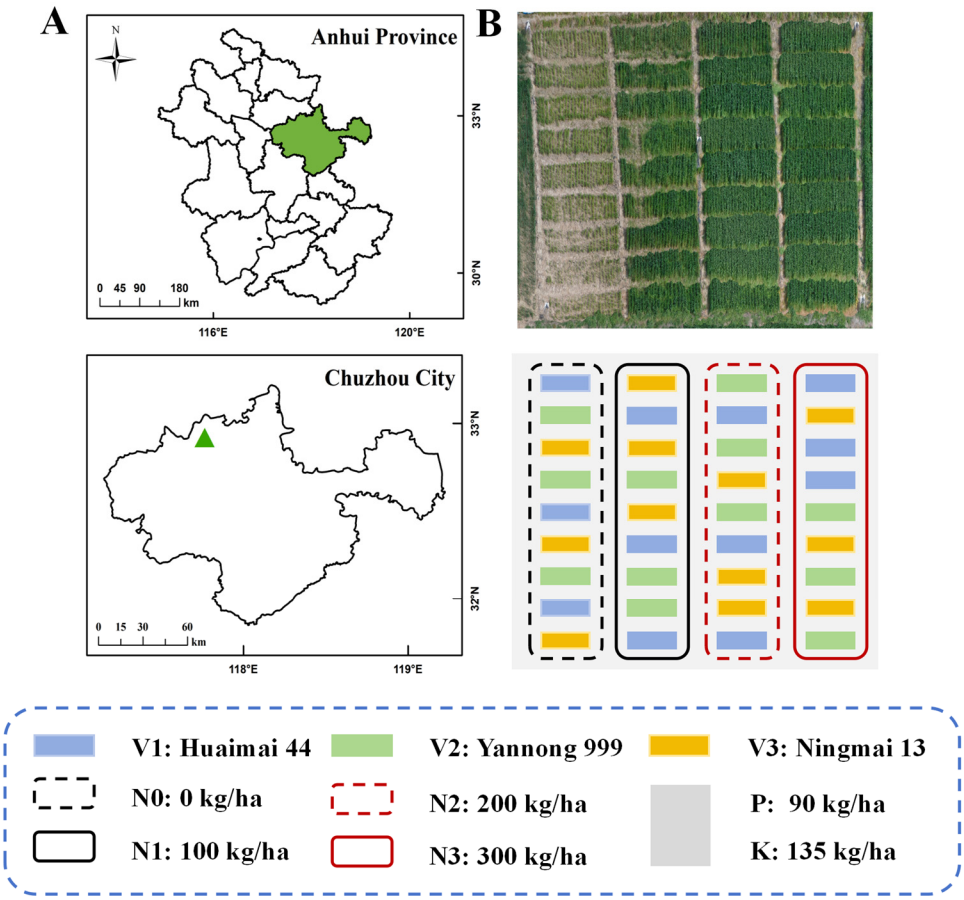

Figure 1. Study area. (**A**) The experiment field was in Chuzhou, Anhui province, China; (**B**) field experimental design.

2.2. Experimental Design

Three nitrogen treatment levels (N0: 0, N1: 100, N2: 200, N3: 300 kg/ha^1) were applied, of which 60% was applied before sowing, and 40% was applied at the jointing stage. Within each fertilizer rate, three wheat varieties were sown: high-gluten wheat HuaiMai 44, high-gluten wheat YanNong 999, and low-gluten wheat NingMai 13 (designated as V1, V2, and V3). Each plot included three replications. The experimental area consisted of 36 subplots, and each subplot was 16 m^2 (2 m × 8 m) in 2021 and 10 m^2 (2 m × 5 m) in 2022. A wheat–rice rotation system was used to explore crop growth differences. Phosphorus fertilizer (P: 90 kg/ha^1) and potash fertilizer (K: 135 kg/ha^1) were applied as basal fertilizer. Field management was the same as that used locally.

2.3. SPAD Data Collection

The collection times of wheat SPAD data were the jointing stage (14 March 2021 and 16 March 2022), the booting stage (8 April 2021 and 10 April 2022), the early filling stage (9 May 2021 and 5 May 2022), and the late filling stage (24 May 2021 and 21 May 2022). A plant nutrient analyzer (TYS-4N, Zhejiang Top Cloud-Agri Technology Co., Ltd., Hangzhou, China) was utilized for these measurements with an accuracy of ±3.0 SPAD and a repeatability of ±3.0 SPAD (SPAD values between 0 and 50). During the measurements, three wheat plants were randomly selected from each plot. For each plant, measurements were taken at the apical leaves' top, middle, and bottom, ensuring the main veins were avoided. The average of the nine points gathered was then used as the SPAD reference value for the plot samples.

2.4. Canopy Spectral Data Acquisition

Wheat canopy spectra were acquired using an ASD FieldSpec HandHeld2 ground spectrometer (Analytical Spectral Devices, Boulder, CO, USA). This spectrometer operates within a wavelength range of 325 to 1075 nm, featuring a wavelength accuracy of ±1 nm and a 25° fully tapered field of view. Data collection coincided with the SPAD measurement between 10:00 am and 2:00 pm on a clear, cloudless day with high light intensity. Before each acquisition, radiometric corrections were performed using a standard reference whiteboard with a reflectance of 0.98. Three representative target areas within each plot were selected for spectral acquisition. The optical fiber input of the spectrometer was positioned vertically at a distance of 50 cm from the plants. Three spectral curves were obtained by scanning each target area once, and the average reflectance value of nine spectral curves was taken as the reference value for the plot.

2.5. Data Processing

2.5.1. Spectral Preprocessing Methods

In this study, the wavelength band of 400 to 900 nm was explicitly selected for analysis to reduce the mechanical noise and baseline drift in the raw spectral data, thereby enhancing the accuracy of the results. The spectral data underwent preprocessing through four distinct methods: Fast Fourier Transform (FFT), Multiplicative Scatter Correction (MSC), Finite Difference (FD), and Savitzky–Golay (SD) smoothing techniques. This process is outlined in the technology roadmap to visualize the sequential steps from data acquisition to model development (Figure 2). First, in this study, based on winter wheat canopy spectral data, we used multiple preprocessing methods (FFT, MSC, FD, and SD) for fusion of different sequence modules and constructed a PLSR prediction model by combining SPAD data separately to determine the optimal combination of preprocessed sequences. On this basis, feature mining methods (CARS, IRIV, and PCA) were used to determine the feature wavelengths, and principal components to further optimize the SPAD prediction model. Finally, the best prediction model was determined by comparing the prediction performance of different models.

The FFT method employs frequency domain analysis for smoothing [48]. The FFT initially transforms the original signal from the spatial domain to the frequency domain. This transformation allows access to the magnitude of the frequency components, which typically exhibit lower magnitudes at high frequencies and greater magnitudes at low frequencies. Subsequently, a low-pass filtering method is applied to eliminate noise by selecting an appropriate cutoff frequency that retains the low-frequency components. The final step involves the application of Inverse Fast Fourier Transform (IFFT) to obtain smoothed spectral data. The FFT filter was executed using Origin 2018 with the cutoff frequency set to 0.1 and the window parameter configured to 5.

MSC [49] is implemented to rectify spectral data for optical path inhomogeneities and scattering associated with physical factors such as sample surface roughness and particle size. The method involves selecting the mean spectrum of all the samples as the reference, from which the mean scattering coefficient was calculated by determining the ratio of the sample spectrum to the reference spectrum. The corrected spectrum was subsequently derived based on the mean scattering coefficient utilizing MATLAB 2021a for computations.

The FD and SD [50] methods were utilized to enhance the resolutions of rapid spectral changes. This functionality assists in the differentiation of overlapping peaks and the extraction of clearer peak information. The calculations of these methods were executed through the software Central Difference feature in Origin 2018. Formula (1), employed for the FD center difference method, is outlined below:

$$f'(x_i) = \frac{f(x_{i+1}) - f(x_{i-1})}{x_{i+1} - x_{i-1}} \quad (1)$$

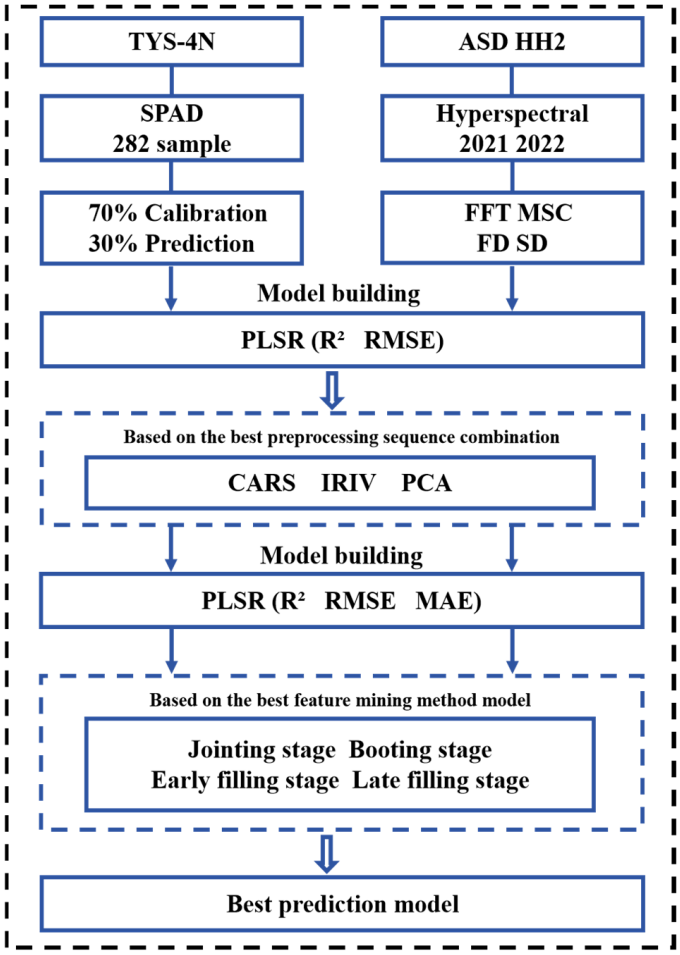

Figure 2. Technology roadmap for winter wheat SPAD prediction model development using canopy hyperspectral data.

For the first and last points of the spectral data, forward differencing (2) or backward differencing (3) was used with the following formulas, respectively:

$$f'(x_i) = \frac{f(x_{i+1}) - f(x_i)}{x_{i+1} - x_i} \quad (2)$$

$$f'(x_i) = \frac{f(x_i) - f(x_{i-1})}{x_i - x_{i-1}} \quad (3)$$

where x is the wavelength, x_i is the wavelength value, x_{i+1} is the wavelength value after x_i, and x_{i-1} is the wavelength value before x_i. In addition, SD is calculated as the second derivative of FD.

Additionally, the approach of fusing multiple preprocessing sequential modules aims to leverage the combination of individual preprocessing methods with distinct spectral processing effects to create a prediction model for SPAD in winter wheat. The multiple preprocessing steps were as follows:

(1) Each preprocessing step is considered an independent module sequentially applied to the raw spectral data. Modular processing is implemented using the Origin software and MATLAB programming language, with data progressing to the next module after processing each module. In this study, FFT and MSC serve as the initial preprocessing modules, with various combinations established alongside FD or SD, such as FFT-MSC-FD and MSC-FFT, reflecting the order of preprocessing.

(2) The fusion of these different sequential modules was utilized to construct SPAD prediction models, which were then compared to prediction models developed using individual preprocessing methods.
(3) The optimal preprocessing sequential module fusion was selected based on evaluations of accuracy and stability across different models.

2.5.2. Feature Mining Methods

To solve the issues of redundancy and high dimensionality inherent in canopy spectral data, this study employed the feature selection methods, Coupled Adaptive Reweighed Sampling (CARS) and Iterative Reweighed Importance Variable (IRIV), alongside the feature extraction technique of Principal Component Analysis (PCA), to reduce dimensionality. This approach enhances the efficiency and accuracy of model construction.

CARS [51,52] is a stepwise weighted sampling feature selection method comprising three phases. Initially, the algorithm generates multiple feature subsets through Monte Carlo sampling, subsequently selecting sample data to construct a Partial Least Squares Regression (PLSR) model while simultaneously updating the weights of each feature. The weight adjustments are facilitated by an exponentially decreasing function, allowing for the ranking and selection of features based on these adjusted weights. Following this, 5-fold cross-validation is performed to access the predictive performance of each subset. Ultimately, the subset characterized by the lowest root mean square error of prediction (RMSEP) is identified as the optimal feature set.

IRIV [53–55] represents an iterative feature mining approach focused on the stepwise selection of critical features for model prediction through systematic weighting and statistical testing. The method starts with the identification of optimal principal components via 5-fold cross-validation. Then, a subset space was constructed for the sub-model using Binary Matrix Sampling (BMS) in each iteration, and the RMSECV for the combination of binary matrices was accessed using Monte Carlo sampling. Variable importance was quantified using the parameters DMEAN (Difference in RMSECV per Variable) and the Mann–Whitney U test. The variables were then categorized as strongly influential, weakly influential, uninformative, or interfering variables, and this process was iterated until no uninformative or confounding variables remained. Finally, backward elimination was employed to refine feature selection, ensuring that the resultant feature set possesses the highest predictive power.

PCA [56,57] is an unsupervised learning method for dimensionality reduction, seeking to generate mutually orthogonal principal components through linear transformations, effectively mapping high-dimensional data into a low-latitude space.

The method starts by decentering the original data to compute the covariance matrix (C) of the adjusted data, which is expressed in Equation (4):

$$C = \frac{1}{n-1} X_{centered}^{T} X_{centered} \quad (4)$$

where n is the number of samples, X is the original data, $X_{centered}$ is the centered data, and $X_{centered}^{T}$ is the transpose of the centered data matrix.

Subsequently, the eigenvalue decomposition of this covariance matrix is performed to obtain latent variables and coefficients. The latent variables are then ranked, and the top k principal components with the largest cumulative explained variance are selected. Finally, the original data were projected onto the space defined by these selected principal components, facilitating dimensionality reduction, as expressed in Equation (5):

$$X_{reduced} = X \times coeff_{selected} \quad (5)$$

where $X_{reduced}$ is the reduced dimension data matrix, X is the original data, and $coeff_{selected}$ is the selected principal component.

2.6. Model Construction and Evaluation

PLSR [58–60] is a statistical method used for multivariate regression analysis to manage multiple linear relationships between independent and dependent variables. The core idea is to develop a regression model that reduces dimensionality by extracting potential variables that can account for variations in both independent and dependent variables. The process can be outlined as follows:

(1) Project the independent and dependent variables into low-dimensional space and identify latent variables that explain their covariance. These latent variables are linear combinations of independent and dependent variables that are orthogonal to each other.
(2) Extract these latent variables to construct a regression model.
(3) Evaluate the model's fit and prediction effects through evaluation indicators such as coefficient of determination (R^2) and root mean square error (RMSE).

In this study, the PLSR algorithm was employed to predict and analyze the SPAD values of the winter wheat canopy, utilizing the spectral data and SPAD values as model inputs. A total of 144 data samples were collected each year, although 141 were deemed suitable due to the presence of outliers, resulting in a total of 282 samples. For modeling purposes, 70% of the sample data were selected as the training set, while 30% were allocated to the validation set to construct the SPAD prediction model for winter wheat. The model accuracy was assessed using three evaluation parameters: coefficient of determination (R^2), root mean square error (RMSE), and mean absolute error (MAE). The formulas for calculations are as follows:

$$R^2 = 1 - \frac{\sum_{i=1}^{n}(x_i - y_i)^2}{\sum_{i=1}^{n}(x_i - \hat{x})^2} \quad (6)$$

$$RMSE = \sqrt{\frac{\sum_{i=1}^{n}(y_i - x_i)^2}{n}} \quad (7)$$

$$MAE = \frac{\sum_{i=1}^{n}|y_i - x_i|}{n} \quad (8)$$

Note: x_i, y_i, and $\hat{x}$ are the actual measured value, predicted value, and average value of the measured data, respectively; n is the number of samples.

3. Results

3.1. Spectral Preprocessing

To better explore the hyperspectral features used for estimating SPAD in wheat, we analyze the spectral variations between the original spectra and those after different methods of preprocessing (Figure 3). The spectral curves of the wheat canopy showed similar trends across growth years, showing an overall pattern of increase followed by a decrease. Notable differences in spectral reflectance were observed at 550 nm, 670 nm, and 720 nm (Figure 3a). The noise present in the FFT-smoothed spectral curves within the 400–500 nm and 800–900 nm ranges was effectively reduced, while the primary trends of the spectral signals were preserved (Figure 3b,c). Meanwhile, when compared to the original spectra, the MSC-treated spectral curves exhibited more concentrated reflectance within the 400–700 nm range, more prominent curve shapes, and enhanced consistency in variation trends (Figure 3d). Furthermore, the reflectance of the FD spectral curve in the 680–750 nm range was amplified, the baseline of the SD spectral curve was flattened, and its variation trend aligned more closely with a horizontal line, resulting in fluctuations concentrated around the peaks and valleys, particularly at 750 nm (Figure 3e,f).

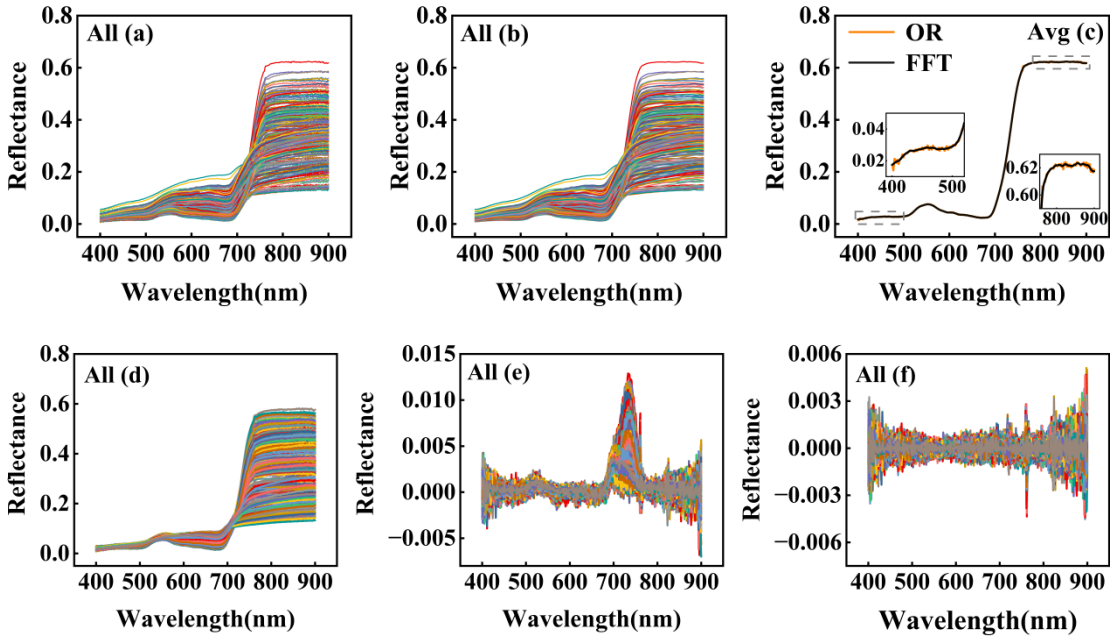

Figure 3. Comparison of spectral curves under different preprocessing methods: (**a**) original spectrum; (**b**) FFT-smoothed spectrum; (**c**) comparison of original and FFT-smoothed spectra; (**d**) MSC spectrum; (**e**) first-order derivative spectrum; (**f**) second-order derivative spectrum. The colored lines represent the spectral reflectance of all samples in the range of 400 nm to 900 nm.

3.2. Accuracy Assessment of Different Preprocessing Methods

To evaluate the performance of single preprocessing methods (FFT, MSC, FD, and SD) and their fusion with different sequence modules to construct PLSR prediction models, in this study, the models were categorized into three groups, C1, C2, and C3, and evaluation metrics such as R^2 and RMSE were compared (Figure 4). The order of the processing techniques in C2 and C3 mirrors the sequence of spectral processing. For instance, the analysis employing FFT-MSC-FD indicates an initial prioritization of the FFT method, followed by the application of MSC on the FFT spectra, and finally, the application of the FD transformation on the FFT-MSC spectra.

In 2021, model C1 (Figure 4a,b) revealed that the MSC-processed spectral reflectance yielded the highest accuracy (R^2 = 0.72 and RMSE = 5.46), with an improvement of 0.02 and a decrease of 0.53 in RMSE compared to the OR model. Conversely, the FFT model exhibited the lowest accuracy (R^2 = 0.64 and RMSE = 6.01). Fusing the two preprocessing methods highlighted the FFT-MSC model as the superior combination, with an R^2 of 0.74, thus representing enhancements of 0.04, 0.02, and 0.10 compared to the R^2 values of the OR, MSC, and FFT models, respectively. In contrast, the MSC-FFT model showed a decline of 0.06 relative to the MSC model R^2, while improving by 0.02 over the FFT model R^2. The analysis showed that FFT-FD improved R^2 by 0.03 over the MSC-FD model, while FFT-SD improved R^2 by 0.02 over the MSC-SD model. These findings underscore the significant contribution of FFT-prioritized spectra in enhancing model prediction accuracy in 2021.

This study compares model accuracy in both 2022 and the fusion year (Figure 4c–f). The results from 2022 indicate that model C1 achieved the highest accuracy with the OR and FD models, both attaining an R^2 of 0.88, followed closely by the MSC model at R^2 = 0.87, while the FFT presented the lowest accuracy, with R^2 = 0.77. This result is slightly different from 2021. After the fusion of FFT and MSC, the R^2 of the FFT-MSC model reached 0.86. Although the prediction accuracy was slightly lower than that of the OR and MSC models, the R^2 was improved by 0.09 and 0.12 compared with the FFT and MSC-FFT models, respectively. At the same time, the study also found that when FFT-MSC was fused with FD or SD, the model performance was poor, with the FFT-MSC-FD model R^2 = 0.80 and RMSE = 6.29, and the FFT-MSC-SD model R^2 = 0.82 and RMSE = 8.66.

In the fusion year C1, the OR model had the highest accuracy (R^2 = 0.82, RMSE = 6.24) and the FFT model had the lowest accuracy (R^2 = 0.66, RMSE = 6.25). However, in C2, the performance of the FFT-MSC model was significantly improved, with R^2 of 0.01, 0.17, and 0.04 higher than that of the single model OR, FFT, and MSC, respectively, and R^2 of 0.17 higher than that of the combined model MSC-FFT. Additionally, this study identified that the performance of the MSC-SD model was sub-optimal during both single and fusion years, with R^2 values of 0.64, 0.76, and 0.64, respectively, and correspondingly high RMSE values of 7.24, 9.91, and 9.88, respectively. In conclusion, the FFT-MSC fusion preprocessing method was selected for subsequent studies based on its superior performance in the comparison of model accuracy.

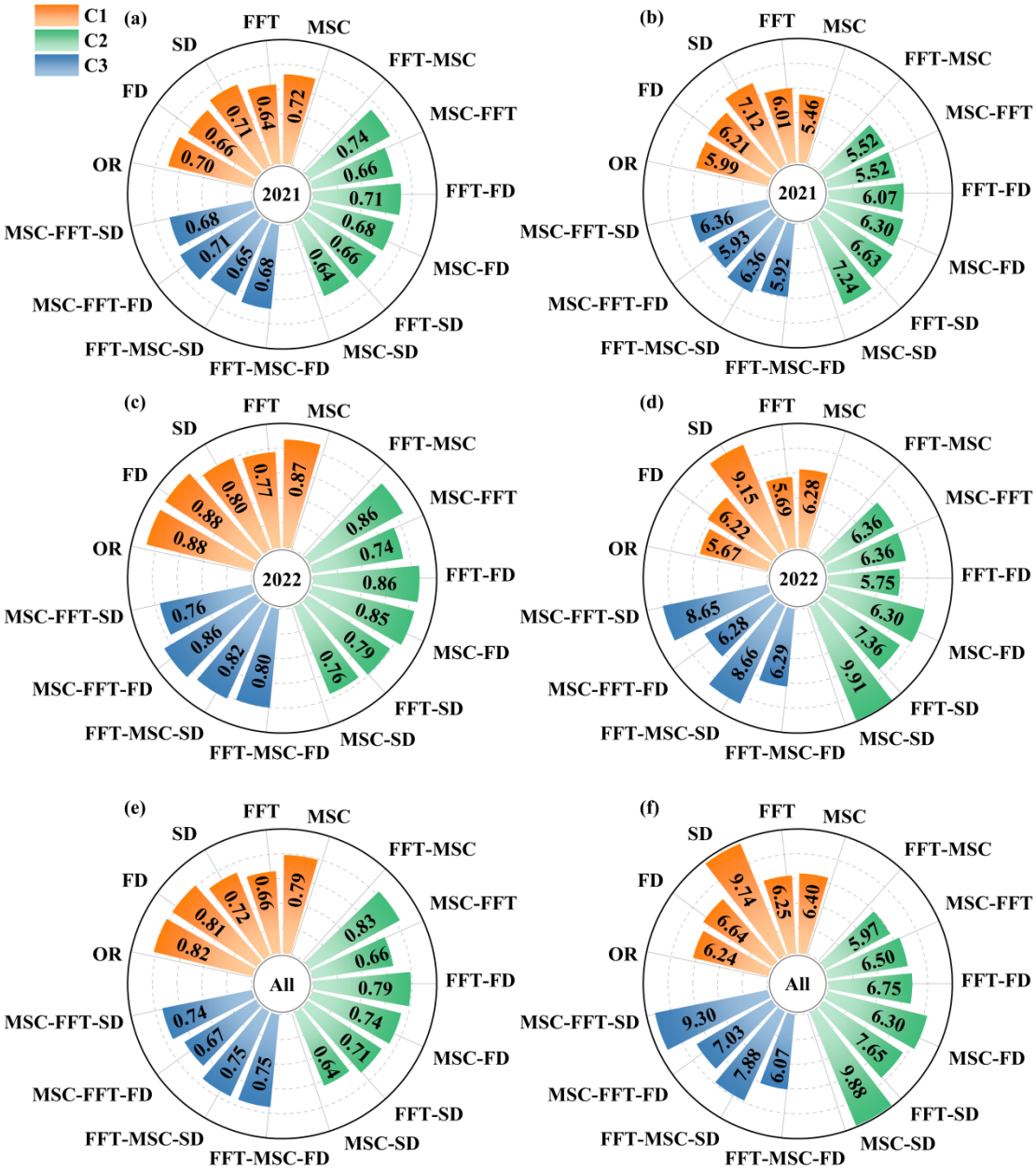

Figure 4. Comparison of modeling accuracy of different preprocessing methods under single and fused growth years: (**a**,**c**,**e**) predictive model validation set R^2; (**b**,**d**,**f**) predictive model validation set RMSE; (**a**,**b**) 2021; (**c**,**d**) 2022; (**e**,**f**) fusion year.

3.3. Spectral Feature Mining Results

In this study, the canopy spectra after FFT-MSC preprocessing were subjected to feature extraction utilizing the CARS and IRIV algorithms for feature selection. The results of the feature band selection, along with their corresponding spectral ranges, are shown in Table 1 and Figure 5.

Table 1. Characteristic wavelength results by single growth year and fusion growth year.

Feature Selection Algorithms	Growth Year	Number	Characteristic Wavelengths (nm)
CARS	2021	17	460, 463, 465, 467, 468, 475, 479, 480, 481, 485, 692, 694, 695, 696, 728, 776, 897
	2022	7	504, 508, 517, 518, 694, 753, 820
	All	18	409, 424, 425, 502, 503, 504, 506, 507, 508, 509, 552, 553, 673, 675, 677, 757, 899, 900
IRIV	2021	12	467, 710, 712, 713, 785, 787, 790, 849, 850, 851, 865, 866
	2022	12	435, 488, 724, 725, 726, 727, 728, 753, 754, 835, 836, 861
	All	26	427, 428, 429, 430, 431, 465, 466, 467, 489, 490, 505, 506, 538, 539, 540, 671, 672, 673, 674, 688, 817, 818, 819, 820, 821, 822

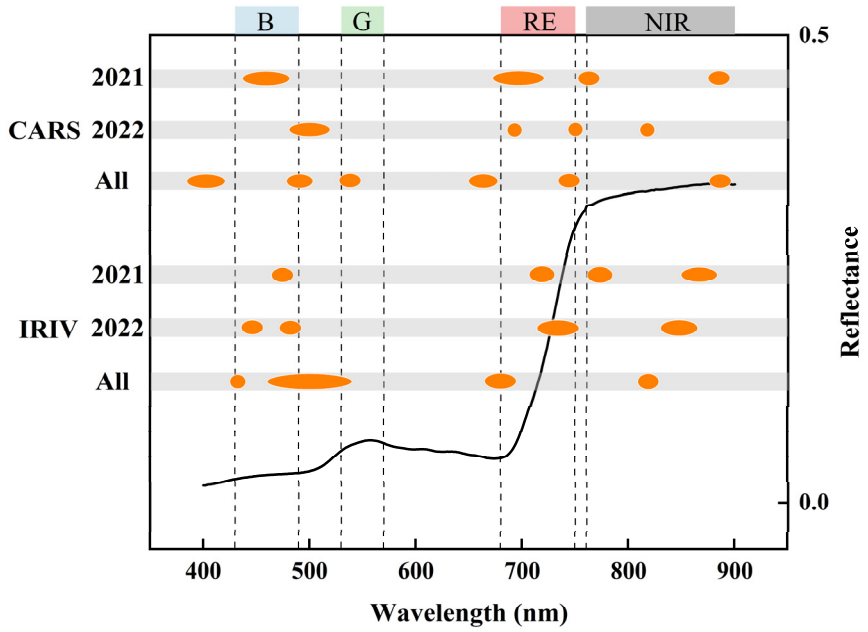

Figure 5. Wavelength selection for winter wheat SPAD prediction using CARS and IRIV methods across different growth years. The selected feature wavelengths in the blue (B), green (G), red-edge (RE), and near-infrared (NIR) regions are shown for 2021, 2022, and fusion years. The orange ellipses indicate the most relevant wavelength bands selected by the feature mining methods. The black line represents the average reflectance curve from 400 to 900 nm across the spectral range.

The characteristic wavelengths selected by CARS in 2021 predominantly fall within the spectral ranges of 460 to 485 nm and 692 to 728 nm, situated in the blue light and red-edge regions, respectively. Additionally, the wavelengths of 776 and 897 nm are classified in the near-infrared region. In 2022, the minimum characteristic wavelengths identified were limited to seven, with 694 nm and 753 nm in the red-edge region, 820 nm in the near-infrared region, and the remaining wavelengths distributed across the blue–green light spectrum. In the fusion year, the characteristic wavelengths predominantly occupied the blue–green and green light regions.

The results of the IRIV feature selection indicate that the characteristic wavelength of 467 nm in 2021 is located in the blue light region, while wavelengths of 710 nm, 712 nm, and 713 nm are within the red-edge region. The remaining wavelengths are confined to the

near-infrared region. Similar patterns are observed for the characteristic wavelengths in 2022, spanning the blue light, red-edge, and near-infrared regions. During the fusion year, the characteristic wavelengths of 505 nm, 506 nm, 538 nm, 539 nm, and 540 nm fall within the blue–green and green light regions, with all remaining wavelengths situated in the blue light, red-edge, and near-infrared regions.

Concerning PCA, the cumulative variance-explained curves for both single and fusion years exhibit a comparable upward trend, demonstrating a systematic increase as the number of principal components increases (Figure 6). The variance accounted for by the first principal component under the single-year analysis surpasses 99%. Conversely, the variance explained by the first principal component during the fusion year reaches only 78%, followed by a sharp increase in the curve, exhibiting an inflection point at the third principal component, beyond which the curve attains a plateau, resulting in a cumulative variance explained exceeding 99%. To enhance the stability and generalization ability of the model, the first three principal components were designated as the independent variables of the subsequent SPAD prediction model.

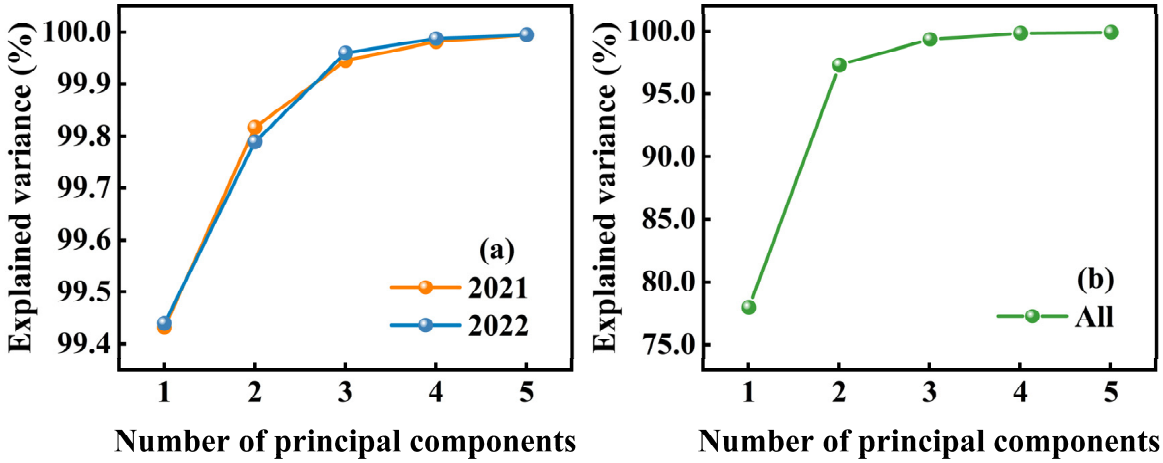

Figure 6. Cumulative explanations of the variance of the first five principal components extracted by PCA: (**a**) 2021 and 2022; (**b**) year of fusion.

3.4. Evaluation of SPAD Prediction Models Based on CARS, IRIV, and PCA

This study evaluated the effectiveness of CARS and IRIV feature selection algorithms and the PCA feature extraction technique in predicting wheat SPAD values (a summary table comparing different preprocessing methods and feature selection algorithm models is shown in Supplementary Materials). The PLSR model is shown in Figure 7. The results indicate that the SPAD prediction model derived from the IRIV algorithm demonstrates superior accuracy. For example, in the fusion year, the SPAD prediction model based on IRIV achieved the highest accuracy, with an R^2 of 0.85, RMSE of 5.61, MAE of 4.43, and standard error (SE) of 0.34. Similarly, for 2021, the IRIV-derived model secured an R^2 of 0.79, RMSE of 5.01, MAE of 4.17, and SE of 0.43. Conversely, the PCA models yielded the lowest accuracy and largest standard error in 2021, with an R^2 value of 0.56, RMSE of 7.21, MAE of 5.59, and SE of 0.63. In addition, further analysis revealed that in 2022, all three algorithms—CARS, IRIV, and PCA—demonstrated optimal performance, with R^2 values of 0.89, 0.89, and 0.84, and corresponding RMSE values of 5.72, 4.51, and 6.74, respectively. The study also found that in the fusion year, the SE values of CARS, IRIV, and PCA models were the smallest, which were 0.36, 0.34, and 0.38, respectively. A comprehensive comparison elucidates that the prediction model derived from IRIV showed the best performance, with the year 2022 marking the peak of predictive accuracy, closely followed by the fusion year.

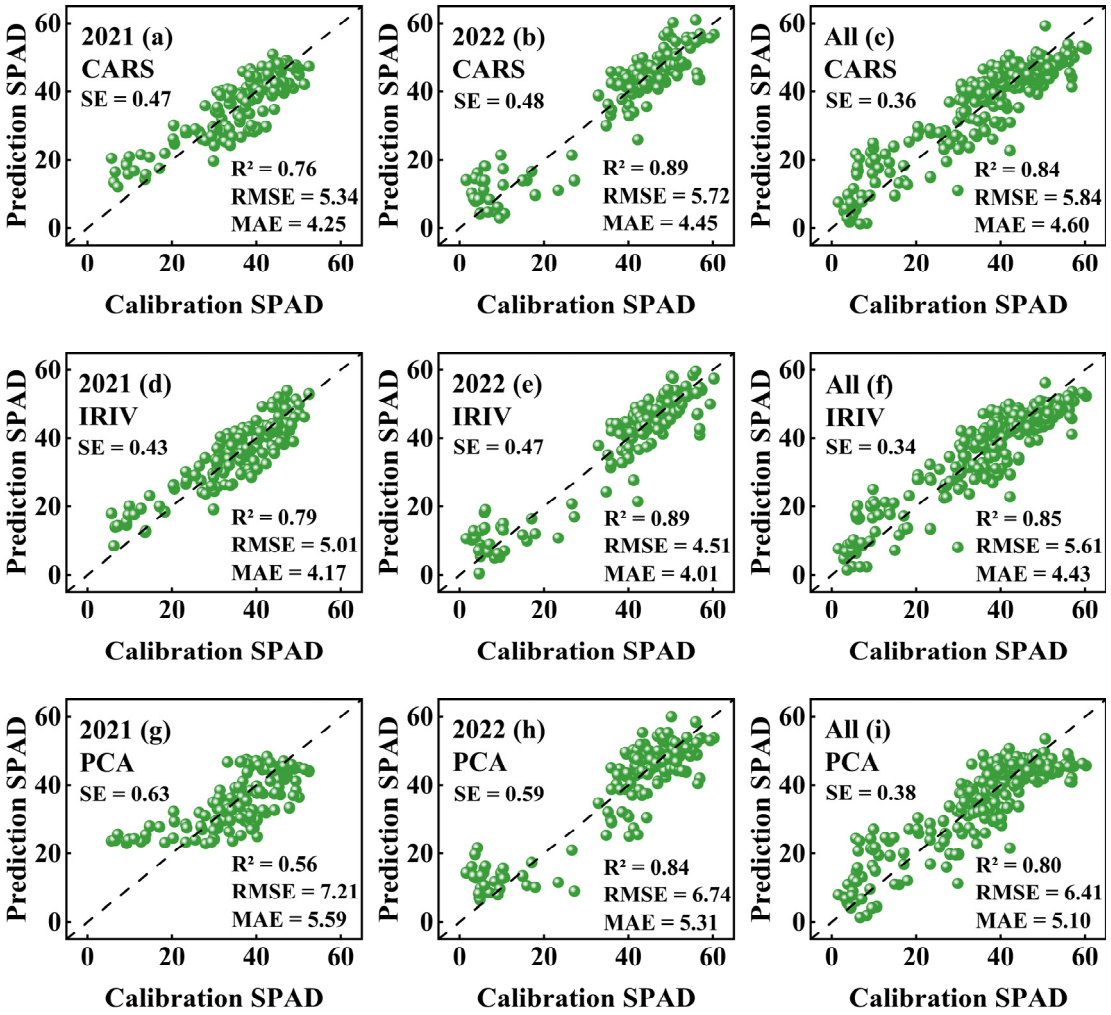

Figure 7. Fitting scatter plots of SPAD prediction models based on different feature mining methods in single years and fused years: (**a**–**c**) CARS prediction model scatter plots; (**d**–**f**) IRIV prediction model scatter plots; (**g**–**i**) PCA prediction model scatter plots.

To account for the multifaceted influence of distinct growth stages on SPAD prediction, this study utilized the fusion year as a case study to develop a linear regression model employing both calibrated and predicted values derived from the IRIV model. Subsequent investigations explored the effect of SPAD prediction across individual growth stages and through the combination of two or three adjacent growth stages.

3.5. Evaluation of SPAD Prediction Model Under Single Growth Stage and Fused Growth Stage

As shown in Table 2, the jointing, booting, early filling, and late filling stages are denoted as S1, S2, S3, and S4, respectively. The combination of booting, jointing, and late filling is designated as S1-S2-S3, etc., when the stages are fused. The results show varying degrees of model accuracy across growth stages, exhibiting an initial increase followed by a decline in predictive performance trend. The accuracy is ranked as follows: S3, S4, S2, and S1, from highest to lowest. Notably, the SPAD value predicted for S3 achieved the highest accuracy, with R^2 = 0.72 and RMSE = 5.58, followed by the S4 model, with R^2 = 0.63, but with poorer robustness, with RMSE = 7.49. When S3 and S4 were fused, the resulting model achieved an R^2 = 0.84, which was enhanced by 0.13 and 0.22 over the individual R^2 values, underscoring its prediction efficacy.

Table 2. Comparison of SPAD prediction models at different growth stages.

Models	Symbol	Growth Stage	R^2	RMSE
Single	S1	Jointing	0.31	4.55
	S2	Booting	0.49	4.57
	S3	Early filling	0.72	5.58
	S4	Late filing	0.63	7.49
Fusion	S1-S2	Jointing-Booting	0.39	4.56
	S2-S3	Booting-Early filling	0.64	5.10
	S3-S4	Early filling-Late filling	0.85	6.57
	S1-S2-S3	Jointing-Booting-Early filling	0.57	4.94
	S2-S3-S4	Booting-Early filling-Late filling	0.85	5.89

Similarly, the S2-S3-S4 model elevated the R^2 by increments of 0.36, 0.13, and 0.22 compared to the S2, S3, and S4 models. However, the anticipated trend observed in previous results did not persist with the inclusion of other single growth stages. For example, the S2-S3 model improved R^2 by 0.15 compared to the S2 model but decreased R^2 by 0.08 relative to the S3 model.

This investigation uncovered a decline in model accuracy when S1 was integrated with other growth stage models; specifically, the S1-S2 model exhibited a decline in R^2 of 0.10 compared to the S2 model, while the S1-S2-S3 model demonstrated a decrease of 0.07 compared to the S2-S3 model. These findings necessitate further exploration of SPAD prediction efficacy across varying growth stages.

4. Discussion

4.1. Winter Wheat SPAD Prediction Based on Different Sequential Fusion of Multiple Preprocesses

The original spectral curves exhibited a general decrease following MSC processing within the visible light spectrum (Figure 3d). The spectral curves of various samples demonstrated increased proximity. This phenomenon is likely attributed to the standardization of each sample's spectra by MSC, addressing baseline drift issues resulting from phenotypic variations among individual plants, affecting light scattering differently, and ultimately enhancing data reliability [61]. Similarly, FFT reduces noise by smoothing the spectral curve [62]. FD and SD can accentuate subtle features in spectral data, enhancing data resolution [63]. However, comparing the efficacy of these four methods solely based on spectral visualization results after different preprocessing techniques is challenging.

Consequently, through modeling, this study evaluates the impact of FFT, MSC, FD, and SD and their various sequential combinations on SPAD prediction accuracy. The findings indicate that the FFT-MSC combination yields the most favorable performance. Conversely, the accuracy of MSC-FFT across different processing sequence combinations of the same method was notably lower, with R^2 discrepancies ranging from 0.08 to 0.17 (Figure 4). These discrepancies are likely attributed to FFT's ability to prioritize isolating signals with distinct frequency components within spectral data, thereby targeting the elimination of high-frequency noise while preserving low-frequency signals [48]. Subsequent processing of spectral data in conjunction with MSC aids in minimizing multi-source interference and enhancing baseline drift correction capabilities [64]. Notably, this study also observed a diminishing trend in model accuracy and reliability with the inclusion of SD in the combination. This observation may be ascribed to SD introducing new noise while amplifying sensitive bands, which not only reduces the signal-to-noise ratio, but also weakens the spectral and SPAD correlation. [65]. Hence, selecting an appropriate combination of preprocessing methods for constructing a wheat SPAD prediction model is imperative for optimizing nitrogen utilization and maximizing yield.

4.2. Wheat SPAD Prediction with Different Feature Mining Methods

In this study, three feature mining methods, CARS, IRIV, and PCA, were selected with the aim of eliminating the potential interference of redundant information in hyperspectral

data for SPAD prediction. Moreover, when modeling with spectral data, employing feature mining techniques can reduce dimensionality and simplify the model structure [66].

In this study, the model's prediction performance, from highest to lowest, varies across different years, with IRIV, CARS, and PCA being the top performers, respectively (Figure 7; Table 1). CARS showcased that Monte Carlo sampling and EDF could identify 17, 7, and 18 characteristic wavelengths, while IRIV retained 12, 12, and 26 characteristic wavelengths with varying influence on SPAD prediction. Notably, CARS selects a more evenly distributed set of feature bands, with about 40% falling within the blue–green light region and closely associated with carotenoids [67]. On the other hand, IRIV tends to choose a more concentrated distribution of feature bands, with approximately 80% falling within the blue light and red-edge regions. The blue light region is crucial for chlorophyll a and b absorption, directly reflecting the plant's chlorophyll concentration [68]. The red-edge region contains valuable plant canopy information due to the rapid decrease in chlorophyll absorption and the sharp increase in reflectance, playing a significant role in SPAD prediction [69]. The disparity in feature band selection between the two algorithms can be attributed to the fact that CARS is centered on adaptive reweighting, aiming to dynamically select the features that contribute the most to the model's predictive performance through repeated sample sampling and feature selection, with a greater emphasis on the overall performance of the full spectrum [70]. Meanwhile, IRIV typically utilizes statistical methods to assess the relationship between individual bands and target variables, focusing on identifying the most informative features within a given band [71].

To fully harness the predictive capabilities of CARS and IRIV, it is essential to attribute the corresponding chemical bonding and physicochemical characteristics to the chosen characteristic wavelengths. The characteristic wavelength at 467 nm in 2021, jointly selected by CARS and IRIV, closely aligns with the first overtone of the C-H bond, correlates with the chlorophyll absorption peak, and indicates photosynthesis efficiency [72]. IRIV selected characteristic wavelengths at 710 nm, 712 nm, 713 nm, 724 nm, 725 nm, 726 nm, 727 nm, and 728 nm, which are situated in the transition region between strong absorption in the red-edge region, and strong reflection in the near-infrared to the red-edge region. These wavelengths are associated with O-H and C-H bonds and typically reflect changes in plant tissue moisture and chlorophyll content [73]. In previous studies, the red-edge band has been identified as crucial for predicting wheat chlorophyll [74,75]. This study found that CARS, under the 2022 and fusion years, mistakenly excluded important characteristic bands in the red-edge region, potentially contributing to lower model accuracy than IRIV. Additionally, it was observed in this study that the increases in the characteristic wavelengths of CARS and IRIV in the fusion year were in the spectral ranges of 409 to 509 nm and 671 to 688 nm, respectively. These increases may be linked to the diverse physiological state of plants across different years, resulting in varied spectral features. Data fusion aids feature mining algorithms in better identifying physiological feature differences, selecting bands that perform well within a single year, and capturing relatively stable bands across years, leading to a more comprehensive feature selection [76].

The difference in model performance may be due to the intrinsic differences in the classes of the three feature mining methods [77]. PCA belongs to the feature extraction technique, which is a linear combination of principal components to reduce the spectral data dimensionality. It mainly focuses on the correlation between the features while ignoring the relationship between the features and the SPAD, and may discard the feature bands that explain less variance but have a stronger correlation with the SPAD [78]. By comparison, CARS and IRIV are feature selection algorithms, which can select features that are strongly correlated with SPAD based on the original spectra [52,53], and IRIV can recognize complex interactions between spectral data and improve the ability of prediction models to capture nonlinear feature bands [79]. In summary, IRIV can more effectively select feature bands for wheat SPAD. The results of this study also further show that accurate feature mining can effectively reduce data redundancy and enhance the saliency

of feature bands, which in turn provides theoretical support and a technical path for feature optimization of hyperspectral data.

4.3. Prediction of SPAD in Wheat in Different Years and Growth Stages

Exploring the applicability of the SPAD prediction model at multiple growth stages facilitates dynamic monitoring over the full life span, capturing key changing characteristics of the crop at different growth stages and providing more comprehensive data support for crop growth status assessment.

In this study, SPAD prediction models were constructed for wheat in 2021, 2022, and fusion years, and the prediction accuracy of different models varied, which may be because the SPAD prediction effect is affected by factors such as crop canopy structure, light condition, and moisture status, which vary from year to year [80]. As shown in Figure 7, the maximum accuracies of the wheat SPAD prediction models all appeared in 2022. From Figure 8, it can be seen that the SPAD values in 2021 were concentrated in the range of 30~50, while those in 2022 were concentrated in the range of 40~60. The spectral curves in 2022 varied more significantly from the red light to the near-infrared region, and the reflectance of the near-infrared region spectra was higher. This may be because the differences in climatic conditions (e.g., temperature, humidity) in different years may lead to different physiological states of the plants, and the characteristics of the spectral response change, thus affecting the predictive ability of the model [81].

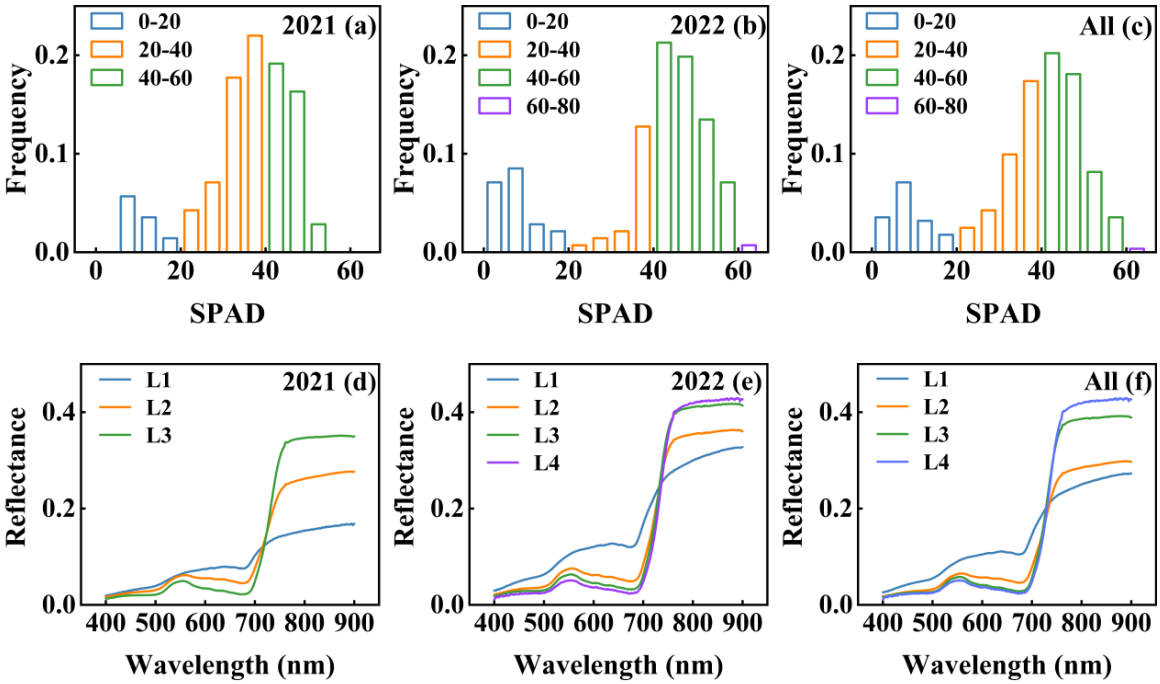

Figure 8. Plots of statistical analysis of SPAD values for single and fused years: (**a**–**c**) histogram of SPAD frequencies; (**d**–**f**) spectral reflectance corresponding to different levels of SPAD.

To further explore the impact of wheat physiological characteristics on the accuracy and robustness of the SPAD prediction model, this study further compared the SPAD prediction effects of the IRIV model at the jointing stage, booting stage, early filling stage, and late filling stage in the fusion years. As shown in Table 2, the model accuracy is compared from high to low, namely, early filling stage, late filling stage, booting stage, and jointing stag. However, the model robustness shows the opposite trend, from high to low, namely the booting stage, jointing stage, early filling stage, and late filling stage. This may be because the leaves in the early filling stage remain green and persistent, which is conducive to yield accumulation [82]. As seen from Table 3, the coefficient of variation (CV) of SPAD was higher in the early and late filling stages, and the significant changes in SPAD

contributed to the excellent fitting of the model [83]. However, at the same time, plant chlorophyll degradation and spectral purity decreased under the influence of tasseling and some withered leaves, which affected the predictive stability of the model [84]. In addition, the model's prediction accuracy in this study was lowest at the jointing stage, which may be because this stage is the transition from plant growth to reproductive growth. Complex physiological changes within the plant lead to significant differences in individual growth and a decrease in the stability of spectral features, affecting the model's construction [85].

Table 3. SPAD statistics at different growth stages in the fusion year.

Growth Stage	Min	Mean	Max	SD	CV (%)
Jointing	30.36	43.34	56.27	5.27	0.12
Booting	26.49	43.01	52.17	5.48	0.13
Early filling	20.60	41.42	60.30	10.42	0.25
Late filling	1.57	16.49	44.29	12.30	0.75

In summary, there were significant differences in the accuracy of SPAD prediction in different years and growth stages. In the mid-growth stage, the SPAD prediction model had high accuracy and good stability, and the regularity of leaf green content changes was strong, and this stage provided a critical monitoring time for precise nitrogen management.

4.4. Limitations and Future Research Perspectives

In this study, a two-year field trial was conducted with winter wheat as the test object. Based on the fusion strategy of multiple preprocessing methods and feature mining techniques, a SPAD prediction model was constructed for different years and growth stages, and a high prediction accuracy was achieved. However, this study still has the following two limitations, which need to be further optimized and expanded.

First of all, the data in this study came from a single crop and test site, so the sample diversity is insufficient, and the results need to be further verified when the growth environment of winter wheat or varieties change. In the future, we will expand the scope of the experiment to increase the sample representativeness, and combine the biomass and nitrogen data of other crops (e.g., rice, maize), so as to further improve the performance and applicability of the predictive model of crop chlorophyll. In addition, the acquisition of winter wheat canopy spectral data is susceptible to weather (e.g., cloudy days, strong winds, etc.), and future research could incorporate multi-temporal observation techniques to improve the quality of the spectral data by fusing data under sunny and cloudy conditions. Secondly, for high-dimensional data, it is difficult for current feature mining methods to capture all potential influences in spectral data, and future work will introduce nonlinear modeling algorithms such as the Convolutional Neural Network (CNN) and Recurrent Neural Network (RNN) to mine deep features. Meanwhile, the computational efficiency of real-time applications is also one of the core directions of the subsequent research, which will be combined with migration learning to realize the rapid adaptation and efficient computation of models among different agricultural environments in the future.

5. Conclusions

This study aimed to enhance the accuracy of SPAD prediction in winter wheat by refining the processing of canopy hyperspectral data. The integrated preprocessing approach effectively addressed noise and high data dimensionality challenges. The FFT-MSC sequential module fusion demonstrated significant effectiveness in predicting SPAD values. The FFT-MSC-PLSR model achieved an R^2 of 0.83 and an RMSE of 5.97, surpassing the MSC-FFT model by improving the R^2 by 0.08 to 0.17 and reducing the RMSE by 0.53. Utilizing FFT as the initial preprocessing step significantly enhanced overall model performance. Feature selection through IRIV was particularly sensitive to wheat chlorophyll, especially within the blue light and red-edge regions. The FFT-MSC-IRIV-PLSR model exhibited the highest prediction accuracy, with R^2 values ranging from 0.79 to 0.89 and an

RMSE of 4.51 to 5.61, while PCA demonstrated the lowest accuracy. The year 2022 offered the best conditions for SPAD prediction, with R^2 values reaching up to 0.89 and RMSE values as low as 4.51. The early filling stage yielded the highest prediction accuracy among various growth stages, with an R^2 of 0.72 and RMSE of 0.58. These findings indicate that sequential fusion preprocessing and feature mining significantly enhance SPAD prediction in winter wheat.

Supplementary Materials: The following supporting information can be downloaded at: https://www.mdpi.com/article/10.3390/agriculture14122258/s1.

Author Contributions: Conceptualization, Y.N. and J.L. (Jikai Liu); methodology, Y.N.; software, X.S.; validation, J.L. (Jikai Liu), Q.M. and X.L.; formal analysis, H.Y.; investigation, J.L. (Jun Li); resources, X.L.; data curation, W.W.; writing—original draft preparation, Y.N.; writing—review and editing, Y.N., S.A. and J.L. (Jikai Liu); visualization, Y.N. and Y.S.; supervision, J.L. (Jikai Liu) and X.L.; project administration, X.L.; funding acquisition, X.L. All authors have read and agreed to the published version of the manuscript.

Funding: This research was funded by scientific research projects in higher education institutions of Anhui Province (no. 2023AH051855; 2022AH051623); National Natural Science Foundation of China (no. 42105175); Sub-project of the National Key Research and Development Plan (2022YFD2301402-3); Anhui Engineering Research Center of Smart Crop Planting and Processing Technology Open Research Project (no. ZHKF03); Anhui Province Agricultural Science and Technology Modernization Pilot County Project (no. 880993, 881121); Anhui Province University Science and Engineering Teachers Enterprise Practice Program Project (224jsqygz62).

Institutional Review Board Statement: This study did not require ethical approval.

Data Availability Statement: Data will be made available upon request.

Acknowledgments: We are grateful to Yongji Zhu for his help in revising the article.

Conflicts of Interest: The authors declare no conflicts of interest.

References

1. Liu, J.; Zhu, Y.; Tao, X.; Chen, X.; Li, X. Rapid Prediction of Winter Wheat Yield and Nitrogen Use Efficiency Using Consumer-Grade Unmanned Aerial Vehicles Multispectral Imagery. *Front. Plant Sci.* **2022**, *13*, 1032170. [CrossRef] [PubMed]
2. Gitelson, A.A.; Viña, A.; Ciganda, V.; Rundquist, D.C.; Arkebauer, T.J. Remote Estimation of Canopy Chlorophyll Content in Crops. *Geophys. Res. Lett.* **2005**, *32*, 2005GL022688. [CrossRef]
3. Li, D.; Hu, Q.; Ruan, S.; Liu, J.; Zhang, J.; Hu, C.; Liu, Y.; Dian, Y.; Zhou, J. Utilizing Hyperspectral Reflectance and Machine Learning Algorithms for Non-Destructive Estimation of Chlorophyll Content in Citrus Leaves. *Remote Sens.* **2023**, *15*, 4934. [CrossRef]
4. Cordon, G.; Lagorio, M.G.; Paruelo, J.M. Chlorophyll Fluorescence, Photochemical Reflective Index and Normalized Difference Vegetative Index during Plant Senescence. *J. Plant Physiol.* **2016**, *199*, 100–110. [CrossRef]
5. Jin, X.; Kumar, L.; Li, Z.; Feng, H.; Xu, X.; Yang, G.; Wang, J. A Review of Data Assimilation of Remote Sensing and Crop Models. *Eur. J. Agron.* **2018**, *92*, 141–152. [CrossRef]
6. Su, X.; Nian, Y.; Shaghaleh, H.; Hamad, A.; Yue, H.; Zhu, Y.; Li, J.; Wang, W.; Wang, H.; Ma, Q.; et al. Combining Features Selection Strategy and Features Fusion Strategy for SPAD Estimation of Winter Wheat Based on UAV Multispectral Imagery. *Front. Plant Sci.* **2024**, *15*, 1404238. [CrossRef]
7. Zhou, W.; Liu, Y.; Ata-Ul-Karim, S.T.; Ge, Q.; Li, X.; Xiao, J. Integrating Climate and Satellite Remote Sensing Data for Predicting County-Level Wheat Yield in China Using Machine Learning Methods. *Int. J. Appl. Earth Obs. Geoinf.* **2022**, *111*, 102861. [CrossRef]
8. Zhou, X.; Yang, M.; Chen, X.; Ma, L.; Yin, C.; Qin, S.; Wang, L.; Lv, X.; Zhang, Z. Estimation of Cotton Nitrogen Content Based on Multi-Angle Hyperspectral Data and Machine Learning Models. *Remote Sens.* **2023**, *15*, 955. [CrossRef]
9. Liu, J.; Zhu, Y.; Song, L.; Su, X.; Li, J.; Zheng, J.; Zhu, X.; Ren, L.; Wang, W.; Li, X. Optimizing Window Size and Directional Parameters of GLCM Texture Features for Estimating Rice AGB Based on UAVs Multispectral Imagery. *Front. Plant Sci.* **2023**, *14*, 1284235. [CrossRef]
10. Tao, H.; Feng, H.; Xu, L.; Miao, M.; Long, H.; Yue, J.; Li, Z.; Yang, G.; Yang, X.; Fan, L. Estimation of Crop Growth Parameters Using UAV-Based Hyperspectral Remote Sensing Data. *Sensors* **2020**, *20*, 1296. [CrossRef]
11. Jararweh, Y.; Fatima, S.; Jarrah, M.; AlZu'bi, S. Smart and Sustainable Agriculture: Fundamentals, Enabling Technologies, and Future Directions. *Comput. Electr. Eng.* **2023**, *110*, 108799. [CrossRef]

12. Su, X.; Nian, Y.; Yue, H.; Zhu, Y.; Li, J.; Wang, W.; Sheng, Y.; Ma, Q.; Liu, J.; Wang, W.; et al. Improving Wheat Leaf Nitrogen Concentration (LNC) Estimation across Multiple Growth Stages Using Feature Combination Indices (FCIs) from UAV Multispectral Imagery. *Agronomy* **2024**, *14*, 1052. [CrossRef]
13. Ivanda, A.; Šerić, L.; Bugarić, M.; Braović, M. Mapping Chlorophyll-a Concentrations in the Kaštela Bay and Brač Channel Using Ridge Regression and Sentinel-2 Satellite Images. *Electronics* **2021**, *10*, 3004. [CrossRef]
14. Zhu, Y.; Liu, J.; Tao, X.; Su, X.; Li, W.; Zha, H.; Wu, W.; Li, X. A Three-Dimensional Conceptual Model for Estimating the Above-Ground Biomass of Winter Wheat Using Digital and Multispectral Unmanned Aerial Vehicle Images at Various Growth Stages. *Remote Sens.* **2023**, *15*, 3332. [CrossRef]
15. Golhani, K.; Balasundram, S.K.; Vadamalai, G.; Pradhan, B. Estimating Chlorophyll Content at Leaf Scale in Viroid-Inoculated Oil Palm Seedlings (*Elaeis guineensis* Jacq.) Using Reflectance Spectra (400 Nm–1050 Nm). *Int. J. Remote Sens.* **2019**, *40*, 7647–7662. [CrossRef]
16. Bhadra, S.; Sagan, V.; Maimaitijiang, M.; Maimaitiyiming, M.; Newcomb, M.; Shakoor, N.; Mockler, T.C. Quantifying Leaf Chlorophyll Concentration of Sorghum from Hyperspectral Data Using Derivative Calculus and Machine Learning. *Remote Sens.* **2020**, *12*, 2082. [CrossRef]
17. Gao, L.; Darvishzadeh, R.; Somers, B.; Johnson, B.A.; Wang, Y.; Verrelst, J.; Wang, X.; Atzberger, C. Hyperspectral Response of Agronomic Variables to Background Optical Variability: Results of a Numerical Experiment. *Agric. For. Meteorol.* **2022**, *326*, 109178. [CrossRef]
18. Li, Y.; Wang, H.; Zhao, H.; Zhang, L. Predicting Leaf Nitrogen Content in Wolfberry Trees by Hyperspectral Transformation and Machine Learning for Precision Agriculture. *PLoS ONE* **2024**, *19*, e0306851. [CrossRef]
19. Zhang, X.; Hou, X.; Su, Y.; Yan, X.; Qiao, X.; Yang, W.; Feng, M.; Kong, H.; Zhang, Z.; Shafiq, F.; et al. Analyzing Protein Concentration from Intact Wheat Caryopsis Using Hyperspectral Reflectance. *Chem. Biol. Technol. Agric.* **2023**, *10*, 83. [CrossRef]
20. Lu, X.; Peng, H. Predicting Cherry Leaf Chlorophyll Concentrations Based on Foliar Reflectance Spectra Variables. *J. Indian Soc. Remote Sens.* **2015**, *43*, 109–120. [CrossRef]
21. Zhang, X.; Feng, M.; Yang, W.; Wang, C.; Guo, X.; Shi, C. Using spectral transformation processes to estimate chlorophyll content of winter wheat under low temperature stress. *Chin. J. Eco-Agric.* **2017**, *25*, 1351–1359. [CrossRef]
22. Pande-Chhetri, R.; Abd-Elrahman, A. De-Striping Hyperspectral Imagery Using Wavelet Transform and Adaptive Frequency Domain Filtering. *ISPRS J. Photogramm. Remote Sens.* **2011**, *66*, 620–636. [CrossRef]
23. Xuan, G.; Jia, H.; Shao, Y.; Shi, C. Protein Content Prediction of Rice Grains Based on Hyperspectral Imaging. *Spectrochim. Acta Part A Mol. Biomol. Spectrosc.* **2024**, *320*, 124589. [CrossRef] [PubMed]
24. Guo, F.; Feng, Q.; Yang, S.; Yang, W. Estimation of Potato Canopy Nitrogen Content Based on Hyperspectral Index Optimization. *Agronomy* **2023**, *13*, 1693. [CrossRef]
25. Guo, Y.; Jiang, S.; Miao, H.; Song, Z.; Yu, J.; Guo, S.; Chang, Q. Ground-Based Hyperspectral Estimation of Maize Leaf Chlorophyll Content Considering Phenological Characteristics. *Remote Sens.* **2024**, *16*, 2133. [CrossRef]
26. Singh, P.; Srivastava, P.K.; Malhi, R.K.M.; Chaudhary, S.K.; Verrelst, J.; Bhattacharya, B.K.; Raghubanshi, A.S. Denoising AVIRIS-NG Data for Generation of New Chlorophyll Indices. *IEEE Sens. J.* **2021**, *21*, 6982–6989. [CrossRef]
27. Zhang, J.; Han, W.; Huang, L.; Zhang, Z.; Ma, Y.; Hu, Y. Leaf Chlorophyll Content Estimation of Winter Wheat Based on Visible and Near-Infrared Sensors. *Sensors* **2016**, *16*, 437. [CrossRef]
28. Zhou, L.; Wu, H.; Jing, T.; Li, T.; Li, J.; Kong, L.; Zhou, L. Estimation of Relative Chlorophyll Content in Lettuce (*Lactuca sativa* L.) Leaves under Cadmium Stress Using Visible—Near-Infrared Reflectance and Machine-Learning Models. *Agronomy* **2024**, *14*, 427. [CrossRef]
29. Ollinger, S.V. Sources of Variability in Canopy Reflectance and the Convergent Properties of Plants. *New Phytol.* **2011**, *189*, 375–394. [CrossRef]
30. Gao, D.; Qiao, L.; An, L.; Sun, H.; Li, M.; Zhao, R.; Tang, W.; Song, D. Diagnosis of Maize Chlorophyll Content Based on Hybrid Preprocessing and Wavelengths Optimization. *Comput. Electron. Agric.* **2022**, *197*, 106934. [CrossRef]
31. Zhang, Y.; Hui, J.; Qin, Q.; Sun, Y.; Zhang, T.; Sun, H.; Li, M. Transfer-Learning-Based Approach for Leaf Chlorophyll Content Estimation of Winter Wheat from Hyperspectral Data. *Remote Sens. Environ.* **2021**, *267*, 112724. [CrossRef]
32. Yang, C.; Xu, J.; Feng, M.; Bai, J.; Sun, H.; Song, L.; Wang, C.; Yang, W.; Xiao, L.; Zhang, M.; et al. Evaluation of Hyperspectral Monitoring Model for Aboveground Dry Biomass of Winter Wheat by Using Multiple Factors. *Agronomy* **2023**, *13*, 983. [CrossRef]
33. Liang, L.; Geng, D.; Yan, J.; Qiu, S.; Di, L.; Wang, S.; Xu, L.; Wang, L.; Kang, J.; Li, L. Estimating Crop LAI Using Spectral Feature Extraction and the Hybrid Inversion Method. *Remote Sens.* **2020**, *12*, 3534. [CrossRef]
34. Wang, T.; Gao, M.; Cao, C.; You, J.; Zhang, X.; Shen, L. Winter Wheat Chlorophyll Content Retrieval Based on Machine Learning Using in Situ Hyperspectral Data. *Comput. Electron. Agric.* **2022**, *193*, 106728. [CrossRef]
35. Jin, J.; Wang, Q. Selection of Informative Spectral Bands for PLS Models to Estimate Foliar Chlorophyll Content Using Hyperspectral Reflectance. *IEEE Trans. Geosci. Remote Sens.* **2019**, *57*, 3064–3072. [CrossRef]
36. Zhang, X.; Sun, H.; Qiao, X.; Yan, X.; Feng, M.; Xiao, L.; Song, X.; Zhang, M.; Shafiq, F.; Yang, W.; et al. Hyperspectral Estimation of Canopy Chlorophyll of Winter Wheat by Using the Optimized Vegetation Indices. *Comput. Electron. Agric.* **2022**, *193*, 106654. [CrossRef]
37. Buschmann, C.; Lenk, S.; Lichtenthaler, H.K. Reflectance spectra and images of green leaves with different tissue structure and chlorophyll content. *Isr. J. Plant Sci.* **2012**, *60*, 49–64. [CrossRef]

38. Feng, Z.; Guan, H.; Yang, T.; He, L.; Duan, J.; Song, L.; Wang, C.; Feng, W. Estimating the Canopy Chlorophyll Content of Winter Wheat under Nitrogen Deficiency and Powdery Mildew Stress Using Machine Learning. *Comput. Electron. Agric.* **2023**, *211*, 107989. [CrossRef]
39. Wang, J.; Zhou, Q.; Shang, J.; Liu, C.; Zhuang, T.; Ding, J.; Xian, Y.; Zhao, L.; Wang, W.; Zhou, G.; et al. UAV- and Machine Learning-Based Retrieval of Wheat SPAD Values at the Overwintering Stage for Variety Screening. *Remote Sens.* **2021**, *13*, 5166. [CrossRef]
40. Chen, S.; Lou, F.; Tuo, Y.; Tan, S.; Peng, K.; Zhang, S.; Wang, Q. Prediction of Soil Water Content Based on Hyperspectral Reflectance Combined with Competitive Adaptive Reweighted Sampling and Random Frog Feature Extraction and the Back-Propagation Artificial Neural Network Method. *Water* **2023**, *15*, 2726. [CrossRef]
41. Su, T.; Liu, X.; Lei, B.; Cao, Z.; Di, J.; Xu, L.; Cui, X. Screening the Characteristic Hyperspectral Wavelength Variables of Peanut Leaves Based on Coupled Algorithms to Predict SPAD Value in Peanut. *Int. J. Remote Sens.* **2024**, *45*, 8334–8354. [CrossRef]
42. Yang, Y.; Nan, R.; Mi, T.; Song, Y.; Shi, F.; Liu, X.; Wang, Y.; Sun, F.; Xi, Y.; Zhang, C. Rapid and Nondestructive Evaluation of Wheat Chlorophyll under Drought Stress Using Hyperspectral Imaging. *Int. J. Mol. Sci.* **2023**, *24*, 5825. [CrossRef]
43. Sudu, B.; Rong, G.; Guga, S.; Li, K.; Zhi, F.; Guo, Y.; Zhang, J.; Bao, Y. Retrieving SPAD Values of Summer Maize Using UAV Hyperspectral Data Based on Multiple Machine Learning Algorithm. *Remote Sens.* **2022**, *14*, 5407. [CrossRef]
44. Yuan, Z.; Ye, Y.; Wei, L.; Yang, X.; Huang, C. Study on the Optimization of Hyperspectral Characteristic Bands Combined with Monitoring and Visualization of Pepper Leaf SPAD Value. *Sensors* **2022**, *22*, 183. [CrossRef]
45. Shen, L.; Gao, M.; Yan, J.; Wang, Q.; Shen, H. Winter Wheat SPAD Value Inversion Based on Multiple Pretreatment Methods. *Remote Sens.* **2022**, *14*, 4660. [CrossRef]
46. Wu, B.; Chen, C.; Kechadi, T.M.; Sun, L. A Comparative Evaluation of Filter-Based Feature Selection Methods for Hyper-Spectral Band Selection. *Int. J. Remote Sens.* **2013**, *43*, 7974–7990. [CrossRef]
47. Jia, M.; Li, W.; Wang, K.; Zhou, C.; Cheng, T.; Tian, Y.; Zhu, Y.; Cao, W.; Yao, X. A Newly Developed Method to Extract the Optimal Hyperspectral Feature for Monitoring Leaf Biomass in Wheat. *Comput. Electron. Agric.* **2019**, *165*, 104942. [CrossRef]
48. Horlick, G. Digital Data Handling of Spectra Utilizing Fourier Transformations. *Anal. Chem.* **1972**, *44*, 943–947. [CrossRef]
49. Chen, Z.-P.; Morris, J.; Martin, E. Extracting Chemical Information from Spectral Data with Multiplicative Light Scattering Effects by Optical Path-Length Estimation and Correction. *Anal. Chem.* **2006**, *78*, 7674–7681. [CrossRef]
50. Demetriades-Shah, T.H.; Steven, M.D.; Clark, J.A. High Resolution Derivative Spectra in Remote Sensing. *Remote Sens. Environ.* **1990**, *33*, 55–64. [CrossRef]
51. Li, H.; Liang, Y.; Xu, Q.; Cao, D. Key Wavelengths Screening Using Competitive Adaptive Reweighted Sampling Method for Multivariate Calibration. *Anal. Chim. Acta* **2009**, *648*, 77–84. [CrossRef]
52. Huan, K.; Chen, X.; Song, X.; Dong, W. Variable Selection in Near-Infrared Spectra: Application to Quantitative Non-Destructive Determination of Protein Content in Wheat. *Infrared Phys. Technol.* **2021**, *119*, 103937. [CrossRef]
53. Yun, Y.-H.; Bin, J.; Liu, D.-L.; Xu, L.; Yan, T.-L.; Cao, D.-S.; Xu, Q.-S. A Hybrid Variable Selection Strategy Based on Continuous Shrinkage of Variable Space in Multivariate Calibration. *Anal. Chim. Acta* **2019**, *1058*, 58–69. [CrossRef] [PubMed]
54. Yun, Y.-H.; Wang, W.-T.; Tan, M.-L.; Liang, Y.-Z.; Li, H.-D.; Cao, D.-S.; Lu, H.-M.; Xu, Q.-S. A Strategy That Iteratively Retains Informative Variables for Selecting Optimal Variable Subset in Multivariate Calibration. *Anal. Chim. Acta* **2014**, *807*, 36–43. [CrossRef] [PubMed]
55. Wei, L.; Yuan, Z.; Yu, M.; Huang, C.; Cao, L. Estimation of Arsenic Content in Soil Based on Laboratory and Field Reflectance Spectroscopy. *Sensors* **2019**, *19*, 3904. [CrossRef]
56. Abdi, H.; Williams, L.J. Principal Component Analysis. *WIREs Comput. Stat.* **2010**, *2*, 433–459. [CrossRef]
57. Liu, H.; Li, M.; Zhang, J.; Sun, H.; Long, Y.; Wu, L.; Zhang, Q. PCA Based Model on Chlorophyll Content Diagnosis of Winter Wheat. *IFAC-PapersOnLine* **2018**, *51*, 643–647. [CrossRef]
58. Helland, I.S. Some Theoretical Aspects of Partial Least Squares Regression. *Chemom. Intell. Lab. Syst.* **2001**, *58*, 97–107. [CrossRef]
59. Huang, X.; Guan, H.; Bo, L.; Xu, Z.; Mao, X. Hyperspectral Proximal Sensing of Leaf Chlorophyll Content of Spring Maize Based on a Hybrid of Physically Based Modelling and Ensemble Stacking. *Comput. Electron. Agric.* **2023**, *208*, 107745. [CrossRef]
60. Chen, S.; Hu, T.; Luo, L.; He, Q.; Zhang, S.; Li, M.; Cui, X.; Li, H. Rapid Estimation of Leaf Nitrogen Content in Apple-Trees Based on Canopy Hyperspectral Reflectance Using Multivariate Methods. *Infrared Phys. Technol.* **2020**, *111*, 103542. [CrossRef]
61. Yuan, X.; Zhang, X.; Zhang, N.; Ma, R.; He, D.; Bao, H.; Sun, W. Hyperspectral Estimation of SPAD Value of Cotton Leaves under Verticillium Wilt Stress Based on GWO–ELM. *Agriculture* **2023**, *13*, 1779. [CrossRef]
62. Inouye, T.; Harper, T.; Rasmussen, N.C. Application of Fourier Transforms to the Analysis of Spectral Data. *Nucl. Instrum. Methods* **1969**, *67*, 125–132. [CrossRef]
63. Li, B.; Xie, W. Adaptive Fractional Differential Approach and Its Application to Medical Image Enhancement. *Comput. Electr. Eng.* **2015**, *45*, 324–335. [CrossRef]
64. Silalahi, D.D.; Midi, H.; Arasan, J.; Mustafa, M.S.; Caliman, J.-P. Robust Generalized Multiplicative Scatter Correction Algorithm on Pretreatment of near Infrared Spectral Data. *Vib. Spectrosc.* **2018**, *97*, 55–65. [CrossRef]
65. Nian, Y.; Su, X.; Yue, H.; Zhu, Y.; Li, J.; Wang, W.; Sheng, Y.; Ma, Q.; Liu, J.; Li, X. Estimation of the Rice Aboveground Biomass Based on the First Derivative Spectrum and Boruta Algorithm. *Front. Plant Sci.* **2024**, *15*, 1396183. [CrossRef]
66. Zebari, R.; Abdulazeez, A.; Zeebaree, D.; Zebari, D.; Saeed, J. A Comprehensive Review of Dimensionality Reduction Techniques for Feature Selection and Feature Extraction. *J. Appl. Sci. Technol. Trends* **2020**, *1*, 56–70. [CrossRef]

67. Kume, A. Importance of the Green Color, Absorption Gradient, and Spectral Absorption of Chloroplasts for the Radiative Energy Balance of Leaves. *J. Plant Res.* **2017**, *130*, 501–514. [CrossRef]
68. Kume, A.; Akitsu, T.; Nasahara, K.N. Why Is Chlorophyll b Only Used in Light-Harvesting Systems? *J. Plant Res.* **2018**, *131*, 961–972. [CrossRef]
69. El-Hendawy, S.; Elsayed, S.; Al-Suhaibani, N.; Alotaibi, M.; Tahir, M.U.; Mubushar, M.; Attia, A.; Hassan, W.M. Use of Hyperspectral Reflectance Sensing for Assessing Growth and Chlorophyll Content of Spring Wheat Grown under Simulated Saline Field Conditions. *Plants* **2021**, *10*, 101. [CrossRef]
70. Li, Q.; Huang, Y.; Song, X.; Zhang, J.; Min, S. Moving Window Smoothing on the Ensemble of Competitive Adaptive Reweighted Sampling Algorithm. *Spectrochim. Acta Part A Mol. Biomol. Spectrosc.* **2019**, *214*, 129–138. [CrossRef]
71. Lu, M.; Wang, H.; Xu, J.; Wei, Z.; Li, Y.; Hu, J.; Tian, S. A Vis/NIRS Device for Evaluating Leaf Nitrogen Content Using K-Means Algorithm and Feature Extraction Methods. *Comput. Electron. Agric.* **2024**, *225*, 109301. [CrossRef]
72. Huang, B.; Li, S.; Long, T.; Bai, S.; Zhao, J.; Xu, H.; Lan, Y.; Liu, H.; Long, Y. Research on Predicting Photosynthetic Pigments in Tomato Seedling Leaves Based on Near-Infrared Hyperspectral Imaging and Machine Learning. *Microchem. J.* **2024**, *204*, 111076. [CrossRef]
73. Raypah, M.E.; Nasru, M.I.M.; Nazim, M.H.H.; Omar, A.F.; Muncan, J.; Zahir, S.A.D.M.; Jamlos, M.F.; Jasim, H.M. Reflectance Spectra for Identifying Stress in Different Parts of Leaf: A Case Study on Oil Palm Seedlings. *Int. J. Remote Sens.* **2024**, *45*, 954–980. [CrossRef]
74. Pan, Y.; Wu, W.; Zhang, J.; Zhao, Y.; Zhang, J.; Gu, Y.; Yao, X.; Cheng, T.; Zhu, Y.; Cao, W.; et al. Estimating Leaf Nitrogen and Chlorophyll Content in Wheat by Correcting Canopy Structure Effect through Multi-Angular Remote Sensing. *Comput. Electron. Agric.* **2023**, *208*, 107769. [CrossRef]
75. Shi, H.; Guo, J.; An, J.; Tang, Z.; Wang, X.; Li, W.; Zhao, X.; Jin, L.; Xiang, Y.; Li, Z.; et al. Estimation of Chlorophyll Content in Soybean Crop at Different Growth Stages Based on Optimal Spectral Index. *Agronomy* **2023**, *13*, 663. [CrossRef]
76. Lahat, D.; Adali, T.; Jutten, C. Multimodal Data Fusion: An Overview of Methods, Challenges, and Prospects. *Proc. IEEE* **2015**, *103*, 1449–1477. [CrossRef]
77. Zang, Z.; Xu, Y.; Lu, L.; Geng, Y.; Yang, S.; Li, S.Z. UDRN: Unified Dimensional Reduction Neural Network for Feature Selection and Feature Projection. *Neural Netw.* **2023**, *161*, 626–637. [CrossRef]
78. Suryakala, S.V.; Prince, S. Investigation of Goodness of Model Data Fit Using PLSR and PCR Regression Models to Determine Informative Wavelength Band in NIR Region for Non-Invasive Blood Glucose Prediction. *Opt. Quantum Electron.* **2019**, *51*, 271. [CrossRef]
79. Bai, Z.; Chen, S.; Hong, Y.; Hu, B.; Luo, D.; Peng, J.; Shi, Z. Estimation of Soil Inorganic Carbon with Visible Near-Infrared Spectroscopy Coupling of Variable Selection and Deep Learning in Arid Region of China. *Geoderma* **2023**, *437*, 116589. [CrossRef]
80. Hunt, E.R., Jr.; Daughtry, C.S.T.; Eitel, J.U.H.; Long, D.S. Remote Sensing Leaf Chlorophyll Content Using a Visible Band Index. *Agron. J.* **2011**, *103*, 1090–1099. [CrossRef]
81. Hatfield, J.L.; Gitelson, A.A.; Schepers, J.S.; Walthall, C.L. Application of Spectral Remote Sensing for Agronomic Decisions. *Agron. J.* **2008**, *100*, S-117–S-131. [CrossRef]
82. Fageria, N.K. Yield Physiology of Rice. *J. Plant Nutr.* **2007**, *30*, 843–879. [CrossRef]
83. Zhang, R.; Yang, P.; Liu, S.; Wang, C.; Liu, J. Evaluation of the Methods for Estimating Leaf Chlorophyll Content with SPAD Chlorophyll Meters. *Remote Sens.* **2022**, *14*, 5144. [CrossRef]
84. Li, J.; Lu, X.; Ju, W.; Li, J.; Zhu, S.; Zhou, Y. Seasonal Changes of Leaf Chlorophyll Content as a Proxy of Photosynthetic Capacity in Winter Wheat and Paddy Rice. *Ecol. Indic.* **2022**, *140*, 109018. [CrossRef]
85. Junker, L.V.; Ensminger, I. Relationship between Leaf Optical Properties, Chlorophyll Fluorescence and Pigment Changes in Senescing *Acer Saccharum* Leaves. *Tree Physiol.* **2016**, *36*, 694–711. [CrossRef]

Disclaimer/Publisher's Note: The statements, opinions and data contained in all publications are solely those of the individual author(s) and contributor(s) and not of MDPI and/or the editor(s). MDPI and/or the editor(s) disclaim responsibility for any injury to people or property resulting from any ideas, methods, instructions or products referred to in the content.